

# Equilibrium non-selfgravitating tori around black holes in parameterised spherically symmetric spacetimes

Marie Cassing<sup>1</sup>, Luciano Rezzolla<sup>1,2,3</sup>

<sup>1</sup>*Institut für Theoretische Physik, Max-von-Laue-Strasse 1, 60438 Frankfurt, Germany*

<sup>2</sup>*Frankfurt Institute for Advanced Studies, Ruth-Moufang-Strasse 1, 60438 Frankfurt, Germany*

<sup>3</sup>*School of Mathematics, Trinity College, Dublin 2, Ireland*

Accepted XXX. Received YYY; in original form ZZZ

## ABSTRACT

Non-selfgravitating equilibrium tori orbiting around black holes have a long history and have been employed in numerous simulations of accretion flows onto black holes and other compact objects. We have revisited the problem of constructing such equilibria starting from spherically symmetric black-hole spacetimes expressed in terms of a fully generic and rapidly converging parameterisation: the RZ metric. Within this framework, we have extended the definitions of all of the quantities characterising these equilibria, starting from the concept of the von Zeipel cylinders and up to the possible ranges of the specific angular momenta that are employed to construct families of tori. Within the allowed space of parameters we have then encountered both standard “single-torus” solutions, but also non-standard “double-tori” solutions. While the properties of the first ones in terms of the presence of a single cusp, of a local pressure maximum and of a varying outer radius, are very similar to those encountered in general relativity, the properties of double-tori solutions are far richer and naturally allow for configurations having the same constant specific angular momentum and hence are potentially easier to produce in nature. The existence of these objects is at present very hypothetical, but if these equilibrium tori were to be observed, they would provide very valuable information on the properties of the spacetime and on its deviation from general relativity.

**Key words:** Black hole physics – Gravitation – Accretion, accretion discs

## 1 INTRODUCTION

The theory of non-geodesic, perfect-fluid, non-selfgravitating, geometrically thick and stationary tori orbiting a black hole has a long history dating back to fundamental work in the 1970s (Fishbone & Moncrief 1976; Abramowicz et al. 1978; Kozłowski et al. 1978). As for any stationary fluid with compact support in a gravitational field, its equilibrium is mainly determined by the balance of gravitational forces, pressure gradients and centrifugal forces. A spherical topology is natural in those configurations in which the contributions coming from the centrifugal force are much smaller than those due to pressure gradients and gravitational forces (e.g., in a star). On the other hand, a toroidal topology is inevitable when the contributions to the force balance coming from the pressure gradients are smaller than those due to the centrifugal and gravitational forces. These are indeed the conditions of the fluid flow which we will consider hereafter.

There are several reasons behind the important role that these configurations have played over the years. Firstly, these configurations are sufficiently simple that their configurations can be constructed almost entirely analytically, thus expanding enormously our ability to investigate radically different configurations (see, e.g., Witzany & Jefremov 2018). Second, because in equilibrium, these tori have been employed for decades as initial conditions in advanced numerical simulations of accretion flows onto black holes (see, e.g., Porth et al. 2019), or neutron stars (see, e.g., Çikintoğlu et al. 2022), as they are subject to instabilities of various types when endowed with

magnetic fields (Abramowicz & Fragile 2013). Third, when taken away from their equilibrium conditions, these tori exhibit an interesting dynamics with quasi-periodic oscillations that can be associated with those that are observed, for instance, in high-mass X-ray binaries (see, e.g., Rezzolla et al. 2003a). Finally, by describing the motion of the fluid very close to the event horizon of the black hole, these tori have the potential of providing important observational information on the properties of the spacetime in regions of strong curvature. It is this last aspect, in particular how the spacetime properties can be imprinted on the characteristics of the equilibrium tori, that we will explore in detail in this paper.

Equilibrium tori around black holes have so far been studied in spacetimes that are either spherically symmetric or axisymmetric in general relativity. Under these conditions, they have been shown to appear under very generic conditions as isolated configurations or – after a suitable work of fine tuning – in complex nested multiple-tori configurations (Pugliese & Stuchlík 2017), where each torus has a *distinct* angular momentum (Pugliese & Stuchlík 2020). The investigations, however, have not been limited to Schwarzschild and Kerr black-hole spacetimes (see Abramowicz & Fragile 2013, for an extensive review) and equilibrium tori have been studied also in other, more exotic spacetimes. For instance, the properties – either equilibrium or dynamical – of geometrically thick tori have been explored in Schwarzschild-de-Sitter spacetimes (Rezzolla et al. 2003b; Stuchlík et al. 2009), in (Newman-Unti-Tamburino) NUT spacetimes (Jefremov & Perlick 2016), in spherically symmetric spacetimes in

$f(R)$ -gravity (Cruz-Ororio et al. 2021), around Kerr black holes with a scalar hair (Gimeno-Soler et al. 2019; Gimeno-Soler et al. 2021; Teodoro et al. 2021b), or more recently in the so-called  $q$ -metric (Faraji & Trova 2021; Memmen & Perlick 2021)<sup>1</sup>. Finally, equilibrium tori also have been investigated around ultra-compact objects different from black holes, such as boson stars (Meliani et al. 2015; Olivares et al. 2020; Teodoro et al. 2021a), or naked singularities in Kerr-de Sitter spacetimes Stuchlík et al. (2015).

All of these works testify both the interest in studying these fluid configurations in general relativity and in other, alternative theories of gravity. We here follow the same interest but focus our attention not on a precise alternative theory of gravity or on an exotic spacetime. Rather, our goal here is to investigate the properties of equilibrium tori in generic and parameterised spherically symmetric spacetimes describing either a black hole or another compact object. While there are several options when considering parameterised spherically symmetric spacetimes, our choice here falls on the Rezzolla-Zhidenko (RZ) metric, which uses compactified (conformal) coordinates and a Padé-expansion in terms of continuous fractions to achieve high accuracy already with a small number of parameters and a straightforward treatment of the expansion. In this way, we are able to offer a very general description of equilibrium tori around black holes and to highlight the existence of a much richer family of tori solutions in black-hole spacetimes that are not Schwarzschild. In particular, we discuss the natural occurrence – in some regions of the possible space of parameters – of double-tori solutions sharing the same specific angular momentum and thus not requiring any fine tuning. Should the existence of these tori become evident through astronomical observations, it would provide very precise information on the properties of the spacetime and on its deviation from general relativity.

Our work is organised as follows. In Sec. 2 we briefly recall the theoretical background and mathematical details necessary to describe equilibrium tori and the von Zeipel cylinders. We describe the RZ-metric and its parametrization in Sec. 3, leaving the exploration of single-torus or double-tori solutions in Secs. 4 and 5, respectively. Finally, we present our summary and the conclusions in Sec. 6.

## 2 THE THEORY OF EQUILIBRIUM TORI

In this Section we briefly recall the essential aspects of a non-geodesic, perfect-fluid, non-selfgravitating, geometrically thick and stationary torus orbiting a black hole. Since the gravitational mass of the torus is assumed to be very small when compared with that of the central black hole, we can exploit the test-fluid approximation and therefore ignore the solution of the Einstein equations, relying simply on the background metric of the given black hole, which we will employ in the calculation of the general-relativistic hydrodynamic equations (see also Font & Daigne 2002; Abramowicz & Fragile 2013; Rezzolla & Zanotti 2013, for more detailed discussions).

### 2.1 von Zeipel cylinders

A fundamental starting point to describe such equilibrium tori is the Newtonian theory of the von Zeipel cylinders, which will also be useful to introduce a number of quantities that will be employed in the remainder of this paper. Besides pressure gradients, the equilibrium

in these tori is made possible by their rotation, which we express in terms of the angular velocity  $\Omega$

$$\Omega := \frac{u^\phi}{u^t} = \frac{d\phi}{dt}. \quad (1)$$

and the corresponding specific angular momentum

$$\ell := -\frac{u_\phi}{u_t}. \quad (2)$$

Using now from a convenient identity for the  $t$ -component of the four-velocity,  $(u^t)^{-2} = -(g_{tt} + 2\Omega g_{t\phi} + \Omega^2 g_{\phi\phi})$ , it is straightforward to obtain that

$$u_t^2 = \frac{g_{t\phi}^2 - g_{tt}g_{\phi\phi}}{g_{\phi\phi} + 2\ell g_{t\phi} + \ell^2 g_{tt}}. \quad (3)$$

After using the symmetries of the problem (i.e., stationarity and axisymmetry), the law of momentum conservation (Euler equation) can be expressed in a very compact form as

$$\partial_\mu \ln |u_t| - \left( \frac{\Omega}{1 - \Omega\ell} \right) \partial_\mu \ell = -\frac{1}{\rho h} \partial_\mu p. \quad (4)$$

where  $p$ ,  $\rho$ , and  $h$  are the pressure, rest-mass density, and the specific enthalpy, respectively. For a barotropic fluid, i.e., a fluid for which  $p = p(\rho)$ , the derivative of the enthalpy is proportional to the derivative of the pressure and, as a consequence, the partial derivatives of pressure and enthalpy commute and cancel each other (Rezzolla & Zanotti 2013). Under these conditions, the following identities can be proven, which constitute the thesis of the relativistic von Zeipel theorem

$$\Omega = \Omega(\ell), \quad (5)$$

and

$$\mathcal{R}^2 := \frac{\ell}{\Omega} = -\frac{\ell(g_{\phi\phi} + g_{t\phi}\ell)}{(g_{t\phi} + g_{tt}\ell)} = \frac{r^3 \sin^2(\theta)}{r - 2M}. \quad (6)$$

where  $\mathcal{R}$  is the so-called von Zeipel (cylindrical) radius and the last expression in Eq (6) refers to a Schwarzschild spacetime.

Stated differently, in stationary and axisymmetric circular flow of a barotropic fluid around a compact object, the surfaces of constant angular velocity  $\Omega$  coincide with the surfaces of constant specific angular momentum  $\ell$ . Such surfaces are also known as von Zeipel cylinders. This theorem was originally formulated in Newtonian gravity and stated that, within a rotating selfgravitating object, isodensity (or isopycnic, i.e., at constant rest-mass density) and isobaric (i.e., at constant pressure) surfaces coincide if and only if the angular velocity is a function of the distance from the rotation axis only (see, e.g., von Zeipel 1924; Tassoul 2007). As a result, the Newtonian von Zeipel cylinders are indeed *cylinders*. In a black-hole spacetime, however, the general-relativistic version of the theorem, which is due to Abramowicz (1971), reveals that this is no longer true and that the von Zeipel cylinders are cylindrical surfaces only asymptotically (Rezzolla & Zanotti 2013). In Sec. 3.1 we will discuss how this theorem varies when considering a generic and parameterised black-hole spacetime.

Another important advantage of barotropic fluids is that the differential  $dp/\rho h$  is an exact differential and the partial derivatives commute  $\partial_r \partial_\theta p = \partial_\theta \partial_r p$ . As a result, the integration of the Euler equation (4) does not depend on the integration path and can be expressed as

$$W_{\text{eff}} - W_{\text{in}} = \ln |u_t| - \ln |(u_t)_{\text{in}}| - \int_{\ell_{\text{in}}}^{\ell} \left( \frac{\Omega}{1 - \Omega\ell'} \right) d\ell', \quad (7)$$

where the index in refers to the “inner-edge” of the disc and  $W_{\text{eff}} := \ln |u_t|$ .

<sup>1</sup> As a distinct class of equilibrium solutions, electrically charged tori have been studied in a Reissner-Nordström spacetime (Kovar et al. 2011) and in a Reissner-Nordström-(anti-)de Sitter spacetime (Kučáková et al. 2011).

## 2.2 General properties of geometrically thick tori

Already in Newtonian gravity, the equilibrium of a stationary rotating fluid with compact support is determined by the balance of three factors: gravitational forces, pressure gradients and centrifugal forces. The relative strength of these forces will determine the geometric properties of the fluid and, in particular, a torus topology will appear if the contributions from pressure gradients are smaller than the contributions from centrifugal and gravitational forces. The calculation of equilibrium tori is particularly simple when the fluid has a constant specific angular momentum

$$\ell = \pm U = \text{const.}, \quad (8)$$

where the  $\pm$  signs in (8) refer to a fluid that is either corotating (+) or counter-rotating (−) with respect to the compact object/black hole. The advantage of tori with a constant specific angular momentum is that, in this case,  $\Omega = \Omega(g_{\mu\nu})$  [see Eqs. (5)–(6)], that is, the fluid angular velocity becomes an expression of the metric functions of spacetime only, and the equipotential surfaces can be computed from the metric coefficients and the constant specific angular momentum.

An equipotential surface that is closed at infinity, i.e.,  $W_{\text{eff}} = 0$ , contains local extrema in the radial coordinate:  $r_{\text{cusp}}$  and  $r_{\text{max}}$ , which mark, respectively, the appearance of a cusp in the effective potential and the location of the pressure (rest-mass density) maximum. At both locations,  $\partial W_{\text{eff}}/\partial r = 0$ , such that the corresponding specific angular momentum at these locations is that of a Keplerian geodesic orbit. If the torus matter fills the outermost closed equipotential surface, then  $r_{\text{cusp}} = r_{\text{in}}$  represents the location on the equatorial plane where such matter can accrete onto the black hole and where the maximum of the effective potential on the equatorial plane is reached. Note that this cusp is similar to the cusp appearing in a “Roche lobe”, with the important difference that in the latter case it corresponds to a single point, while here to a whole circle in view of the axisymmetric nature of these tori. On the other hand, the minimum of the effective potential  $W_{\text{eff}}$  is reached at  $r_{\text{max}}$  and the fluid around this location is in a stable equilibrium, such that, if perturbed, it will oscillate around the corresponding radial or polar epicyclic frequency (Rezzolla et al. 2003a).

In general, the choice of the (constant) specific angular momentum will then determine the location of the inner edge of the torus,  $r_{\text{in}}$ , which can be set to be between  $r_{\text{cusp}}$  and  $r_{\text{max}}$ ; clearly  $W_{\text{eff},\text{in}} \leq W_{\text{eff},\text{cusp}}$ . The torus will also be limited in the radial direction by  $r_{\text{out}}$ , which is also the radial location where  $W_{\text{eff},\text{out}} = W_{\text{eff},\text{in}}$ . Note that in the region:  $r_{\text{in}} < r < r_{\text{max}}$ , the specific angular momentum is larger than the Keplerian specific angular momentum  $\ell > \ell_{\text{Kep}}$  and the orbital motion of the fluid is therefore super-Keplerian in the inner part of the torus. On the other hand, the opposite is true in the region  $r_{\text{max}} < r < r_{\text{out}}$ , i.e.,  $\ell < \ell_{\text{Kep}}$ , such that the orbital motion of the fluid is sub-Keplerian in the outer parts of the torus. Clearly, in these regions the pressure gradients in the torus are needed to balance the excess centrifugal acceleration.

Figure 1 collects in a single plot the whole set of possible tori solutions in a Schwarzschild spacetime having constant specific angular momentum. The latter is taken to range between the specific angular momenta of the marginally stable orbit  $\ell_{\text{ms}} = 3.6738$  and of the marginally bound orbit  $\ell_{\text{mb}} = 4$  (Font & Daigne 2002; Rezzolla & Zanotti 2013). More specifically, shown via a colourmap is the value of the effective potential as a function of the conformal coordinate  $x$  for different values of the specific angular momentum. Marked with different lines are the most important properties of the torus, namely: the radial position of the cusp  $r_{\text{cusp}}$  (orange line), the radial position of the pressure maximum  $r_{\text{max}}$  (purple line), and the

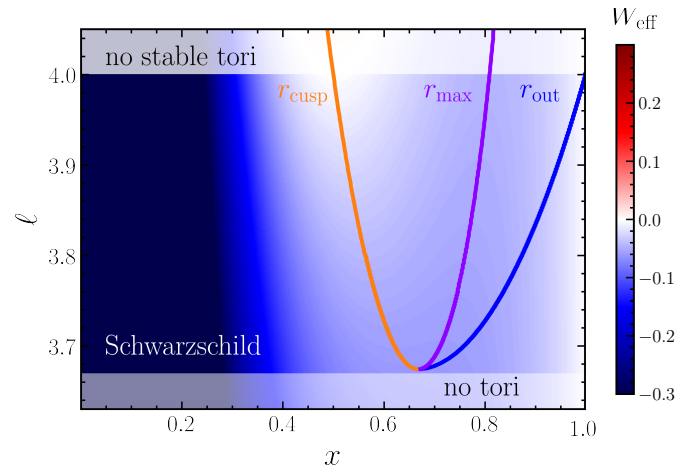


**Figure 1.** Colourmap of the effective potential  $W_{\text{eff}}$  shown as a function of the conformal radial coordinate  $x$  and of the specific angular momentum  $\ell$  for the Schwarzschild spacetime. The figure reports all of the possible tori solutions that can be built with a constant specific angular momentum. Shown with a solid lines are respectively: the location of the cusp of the torus  $r_{\text{cusp}}$  (orange), of the maximum pressure  $r_{\text{max}}$  (purple), and of the outer edge of the torus  $r_{\text{out}}$  (blue). Transparent regions refer to situations in which the specific angular momentum is either larger than that of the marginally bound orbit,  $\ell > \ell_{\text{mb}}$  (top part) or where the specific angular momentum is smaller than that of the marginally stable orbit  $\ell < \ell_{\text{ms}}$  (bottom part); no tori can be built in these regions.

radial position of the outer edge of the torus  $r_{\text{out}}$  (blue line). Using Fig. 1, which to the best of our knowledge has not been presented before, it is straightforward to appreciate a number of salient aspects of tori in a Schwarzschild spacetime. First, the cusp moves towards the event horizon as the specific angular momentum is increased. Second, in contrast to the cusp, the position of the pressure maximum moves outwards with increasing  $\ell$ . Finally, the outer radius of the torus also moves out to larger and larger radii, reaching spatial infinity ( $x = 1$ ) for the maximum value of the specific angular momentum. Two remarks are worth making. First, when the specific angular momentum is larger than the one at the marginally bound orbit, i.e., for  $\ell > \ell_{\text{mb}}$ , the tori are effectively accreting in the sense that the outermost equipotential surfaces will connect with the event horizon without crossing the cusp [see, e.g., , Fig. 11.8 of Rezzolla & Zanotti (2013)]. Under these conditions, in fact, the maximum of the effective potential  $W_{\text{eff}}$  is larger than the corresponding value at spatial infinity; because of this, we indicate this region with the label “no stable tori”. Second, if the specific angular momentum is below the value of the marginally stable orbit of  $\ell < \ell_{\text{ms}}$  no equilibrium tori can be constructed and indeed when  $\ell \rightarrow \ell_{\text{ms}}^+$ , the three fundamental scales of the torus, namely,  $r_{\text{cusp}}$ ,  $r_{\text{max}}$  and  $r_{\text{out}}$  coincide; we indicate this region with the label “no tori”.

## 3 EQUILIBRIUM TORI IN THE RZ-METRIC

We recall that the Rezzolla-Zhidenko (RZ) metric (Rezzolla & Zhidenko 2014) can describe accurately arbitrary spherically symmetric and asymptotically flat spacetimes representing either black-holes – obtained in different theories of gravity – or other compact objects (e.g., naked singularities or boson stars) (Kocherlakota & Rezzolla 2020). It does so by exploiting the rapidly converging properties of a Padé expansion expressed in terms of a continuous fraction so that a

small (i.e.,  $\lesssim 4 - 5$ ) number of parameters is sufficient to reproduce most of the spacetime metrics with percent precision (Konoplya & Zhidenko 2020a; Kocherlakota & Rezzolla 2020). Such parameters can be chosen such that they incorporate deviations from general relativity and can be constrained by experimental observations (Rezzolla & Zhidenko 2014). The RZ parametrization solves difficulties of other parametrizations, which normally have difficulties in isolating the dominant terms within the corresponding parametrization, so that a very large number of parameters is required, all with similar strength (see, e.g., Cardoso et al. 2014). Since its development the RZ-metric has found a number of applications (see, e.g., Völkel et al. 2020; Suvorov & Völkel 2021a; Bauer et al. 2021; Kocherlakota & Rezzolla 2022b) and some extensions of the metric have been made in (see, e.g., Kokkotas et al. 2017; Konoplya & Zhidenko 2020b; Konoplya et al. 2020; Bronnikov et al. 2021). The RZ-metric has been also used in studies of quasi-normal modes (Völkel & Kokkotas 2019; Suvorov & Völkel 2021b; Konoplya & Zhidenko 2022), and more recently, it has played an important role in the theoretical interpretation of the supermassive black-hole images of M87\* (Kocherlakota et al. 2021) and of Sgr A\* (Event Horizon Telescope Collaboration et al. 2022b).

In 2016, the spherically symmetric framework was extended to axisymmetric black holes and generic compact-object stationary spacetimes (Konoplya et al. 2016). This was accomplished by developing two different expansions: *i*) a continued-fraction expansion in terms of a compactified radial coordinate and *ii*) a Taylor expansion in terms of the cosine of the polar angle. Both have a fast convergence and in the polar direction there is an exact limit on the equatorial plane. Calculations of black holes shadow images in this axisymmetric KRZ-metric have been performed by Younsi et al. (2016) and the Blandford-Znajek mechanism (Blandford & Znajek 1977) has been investigated by Konoplya et al. (2021). A test of the KRZ-metric has been done with iron  $K\alpha$ -lines by Ni et al. (2016), with X-ray reflection spectroscopy by (Nampalliwar et al. 2020; Abdikamalov et al. 2021; Yu et al. 2021) or with gravitational-wave observations (Shashank & Bambi 2022). Furthermore, Siqueira & Richartz (2022) have considered the KRZ parametrization to describe a Kerr-like black hole surrounded by a massive scalar field.

In what follows, we briefly review the most salient aspects of the RZ approach. Using spherical polar coordinates  $(t, r, \theta, \phi)$  the RZ metric has the generic form (Rezzolla & Zhidenko 2014)

$$ds^2 = -N^2(r)dt^2 + \frac{B^2(r)}{N^2(r)}dr^2 + r^2d\Omega^2, \quad (9)$$

where  $d\Omega^2 = d\theta^2 + \sin^2(\theta)d\phi^2$  is the line element of a sphere. This metric is more conveniently expressed in terms of the coordinates  $(t, x, \theta, \phi)$ , where  $x$  is the compactified radial coordinate defined as

$$x := 1 - \frac{r_0}{r}, \quad (10)$$

which maps the infinite interval  $r \in [r_0, \infty)$  between the event horizon at  $r_0$  and spatial infinity to the finite interval  $x \in [0, 1)$ . At the horizon, the value of the metric function  $N$  must be zero  $N(r_0) = 0$ . This boundary condition is implicit for the Ansatz in the compactified coordinate  $x$  as:

$$N^2 = xA(x), \quad (11)$$

where  $A(x) > 0$  for  $0 \leq x \leq 1$ . After introducing the near horizon parameters  $\epsilon, a_0, b_0$  the functions  $A(x)$  and  $B(x)$  can be expressed as

$$A(x) = 1 - \epsilon(1-x) + (a_0 - \epsilon)(1-x)^2 + \tilde{A}(x)(1-x^3), \quad (12)$$

$$B(x) = 1 + b_0(1-x) + \tilde{B}(x)(1-x)^2. \quad (13)$$

Here  $\tilde{A}(x)$  and  $\tilde{B}(x)$  characterize the near horizon properties of the metric, i.e., at  $x \approx 0$  and the properties at spatial infinity, i.e., at  $x \approx 1$ . They can be parametrized in terms of a Padé-expansion as

$$\tilde{A}(x) = \frac{a_1}{1 + \frac{a_2x}{1 + \frac{a_3x}{1 + \dots}}}, \quad (14)$$

$$\tilde{B}(x) = \frac{b_1}{1 + \frac{b_2x}{1 + \frac{b_3x}{1 + \dots}}}, \quad (15)$$

where, at the horizon, we neatly have that

$$\tilde{A}(0) = a_1, \quad \tilde{B}(0) = b_1. \quad (16)$$

An important and highly effective feature of the RZ expansion is that if any of the coefficients  $a_i$  and  $b_i$  with  $i \geq 1$  is zero, all the others are automatically zero, such that the truncation of the expansion is sharp from that order on.

### 3.1 Equilibrium tori in the RZ-metric

Recalling the theory of the von Zeipel cylinders reviewed in Sect. 2.1, we know that the relevant expressions to describe the tori do not depend on the  $g_{rr}$  metric function and therefore are independent of the function  $B(x)$  in the metric (9). As a result, the expression for the  $t$ -component of the 4-velocity is given by

$$u_t^2 = \frac{x A(x) r_0^2 \sin^2(\theta)}{-(1-x)^2 x A(x) \ell^2 + r_0^2 \sin^2(\theta)}, \quad (17)$$

while the acceleration has the generic covariant components

$$a_\mu = \frac{1}{2} \frac{\partial_\mu(-N^2(x)) + \Omega^2 \partial_\mu \left( r_0^2 \sin^2(\theta) / (1-x)^2 \right)}{-N^2(x) + \Omega^2 \left( r_0^2 \sin^2(\theta) / (1-x)^2 \right)}. \quad (18)$$

From these quantities and recalling that the acceleration must vanish for a particle moving on a Keplerian circular orbit, it is possible to derive the expression of the Keplerian angular velocity as

$$\Omega_{\text{Kep}} := \left( \frac{u_\phi}{u^t} \right)_{\text{Kep}} = \pm \sqrt{\frac{A(x) + x A'(x)}{2r_0^2 / (1-x)^3}}, \quad (19)$$

while the corresponding expression for the Keplerian specific angular momentum is

$$\ell_{\text{Kep}}(x) := - \left( \frac{u_\phi}{u^t} \right)_{\text{Kep}} = \pm \frac{r_0}{x} \sqrt{\frac{A(x) + x A'(x)}{2(1-x)A^2(x)}}. \quad (20)$$

Under these conditions and a metric that is diagonal (as the RZ metric), the equation of the von Zeipel cylinders reduces to the known relation between  $\ell$  and  $\Omega$ , i.e.,

$$\begin{aligned} g_{tt}\ell + g_{t\phi}(1 + \Omega\ell) + \Omega g_{\phi\phi} &= 0, \\ g_{tt}\ell &= -\Omega g_{\phi\phi}. \end{aligned} \quad (21)$$

such that the von Zeipel radius (squared) in the RZ-metric is given by

$$\mathcal{R}_{\text{vZ}}^2 := \frac{\ell}{\Omega} = - \frac{g_{\phi\phi}}{g_{tt}} = \frac{r_0^2 \sin^2(\theta)}{(1-x)^2 N^2(x)}. \quad (22)$$

Furthermore, the effective potential in the RZ-metric – expressed in terms of  $x$  and  $\theta$  coordinates – reads as follows with the last expression referring to the potential at the Keplerian angular momentum.

$$\begin{aligned} W_{\text{eff}}(x) &= \ln |u_t| \\ &= \frac{1}{2} \ln \left| \frac{x A(x) r_0^2 \sin^2(\theta)}{-(1-x)^2 x A(x) \ell^2 + r_0^2 \sin^2(\theta)} \right| \\ &= \frac{1}{2} \ln \left( \frac{x A}{1 \mp ((1-x)(A + x A')) / (2x(1-x)A)} \right). \end{aligned} \quad (23)$$

$$u_t^2 = \frac{x(1-\epsilon(1-x) + (a_0 - \epsilon)(1-x)^2 + a_1(1-x)^3) r_0^2 \sin^2(\theta)}{-x((1-x)^2 - \epsilon(1-x)^3 + (a_0 - \epsilon)(1-x)^4 + a_1(1-x)^5) \ell^2 + r_0^2 \sin^2(\theta)} \quad (24)$$

$$\Omega_{\text{Kep}} = \pm \sqrt{\frac{(1-x)^3 [1 + \epsilon(-2 + 6x - 3x^2) + a_0(1 - 4x + 3x^2) + a_1(1 - 6x + 9x^2 - 4x^3)]}{2r_0^2}} \quad (25)$$

$$\ell_{\text{Kep}} = \pm \frac{r_0}{x} \sqrt{\frac{1 + \epsilon(-2 + 6x - 3x^2) + a_0(1 - 4x + 3x^2) + a_1(1 - 6x + 9x^2 - 4x^3)}{2(1-x) [1 - \epsilon(1-x) + (a_0 - \epsilon)(1-x)^2 + a_1(1-x)^3]}} \quad (26)$$

$$W_{\text{eff}}(x) = \frac{1}{2} \ln \left( \frac{x(1-\epsilon(1-x) + (a_0 - \epsilon)(1-x)^2 + a_1(1-x)^3)}{1 \mp (1-x) [1 - \epsilon(2 - 6x + 3x^2) + a_0(1 - 4x + 3x^2) + a_1(1 - 6x + 9x^2 - 4x^3)] [2x(1-\epsilon(1-x) + (a_0 - \epsilon)(1-x)^2 + a_1(1-x)^3)]^{-1}} \right) \quad (27)$$

$$\mathcal{R}_{\text{vZ}}^2 = \frac{r_0^2 \sin^2(\theta)}{x [(1-x)^2 - \epsilon(1-x)^3 + (a_0 - \epsilon)(1-x)^4 + a_1(1-x)^5]} \quad (28)$$

### 3.2 Constraints on the range of parameters of the RZ-metric

Although the expressions presented above are given in terms of three RZ coefficients  $\epsilon$ ,  $a_1$  and  $a_2$  and that these coefficients are presently unknown, it is worth noting that post-Newtonian (PN) experiments in the solar system already provide some constraints on at least one of them. In particular, the experiments suggest that the parameterised post-Newtonian coefficients  $\beta$  and  $\gamma$  are constrained to be (Will 2006)

$$|\beta - 1| \lesssim 2.3 \times 10^{-4}, \quad |\gamma - 1| \lesssim 2.3 \times 10^{-5}, \quad (29)$$

such that

$$a_0 = (\beta - \gamma) \frac{2M^2}{r_0^2} \simeq 10^{-4}, \quad (30)$$

and can be reasonably assumed to be zero in a first approximation (see below).

For the RZ parameters considered here, analytical bounds can be derived on the possible range of values and these have been presented in a number of studies and recently been summarised by Kocherlakota & Rezzolla (2022a). We next briefly review them also in connection to the existence of solutions of non-selfgravitating tori. We start by recalling that the condition for the presence of an event horizon in the RZ-metric is  $N(r_0) = 0$ . Outside the outermost horizon the function  $N(r)$  has to be positive and therefore  $A(x) > 0$ . Furthermore, the square of the specific angular momentum has to be positive, such that using expression (20) we find that

$$A(x) + xA'(x) > 0 \quad \text{for } x \in [0, 1]. \quad (31)$$

#### 3.1.1 Analytical expressions for $\epsilon$ , $a_0$ and $a_1$

Expressions (19)–(23) are obtained in the RZ-metric but otherwise generic, that is, not restricted to a finite set of coefficients  $\epsilon$  and  $a_i$ . In practice, however, we need to truncate the infinite expansion (15) to a finite (and possibly small) set of coefficients. In this case, setting  $a_2 = 0$  and taking into account the coefficients  $\epsilon$ ,  $a_0$ ,  $a_1$  we obtain the following expressions for the four-velocity, the angular velocity, the specific angular momentum, the von Zeipel (squared) radius and the effective potential

Evaluating the condition (31) at  $x = 0$  and  $x = 1$  we obtain the following constraints on the parameters  $\epsilon$ ,  $a_0$ , and  $a_1$

$$a_1 \geq -1 + 2\epsilon - a_0, \quad (32)$$

$$\epsilon > -1. \quad (33)$$

To find the range of allowed parameters  $\epsilon$ ,  $a_0$ ,  $a_1$  we look at the behaviour of the metric functions in a boundary case. For example, when  $\epsilon = 0$ ,  $a_0 = 0$  and  $a_1 \neq 0$ , we obtain that the largest allowed value of  $a_1$  for the specific angular momentum to be positive is  $a_1 = 4$ .

To find an analytic expression for the upper boundary of  $a_1$  we consider the condition that the minimum  $x_m$  of the function  $A(x) + xA'(x)$  has to be positive, i.e.,

$$A(x_m) + x_m A'(x_m) \geq 0. \quad (34)$$

The minimum is found analytically to be at

$$\begin{aligned} x_{m\pm} &= \left( \frac{9a_1 - 3\epsilon + 3a_0}{12a_1} \right) \\ &\pm \sqrt{\left( \frac{9a_1 + 3a_0 - 3\epsilon}{12a_1} \right)^2 + \left( \frac{3\epsilon - 2a_0 - 3a_1}{6a_1} \right)}. \end{aligned} \quad (35)$$

For the derivation of this condition the following expressions have been used:

$$\begin{aligned} F(x) &= A(x) + xA'(x) \\ &= 1 + \epsilon(-2 + 6x - 3x^2) + a_0(1 - 4x + 3x^2) \\ &\quad + a_1(1 - 6x + 9x^2 - 4x^3), \end{aligned} \quad (36)$$

and

$$F'(x) = 6\epsilon(1-x) + a_0(6x-4) + a_1(-6+18x-12x^2). \quad (37)$$

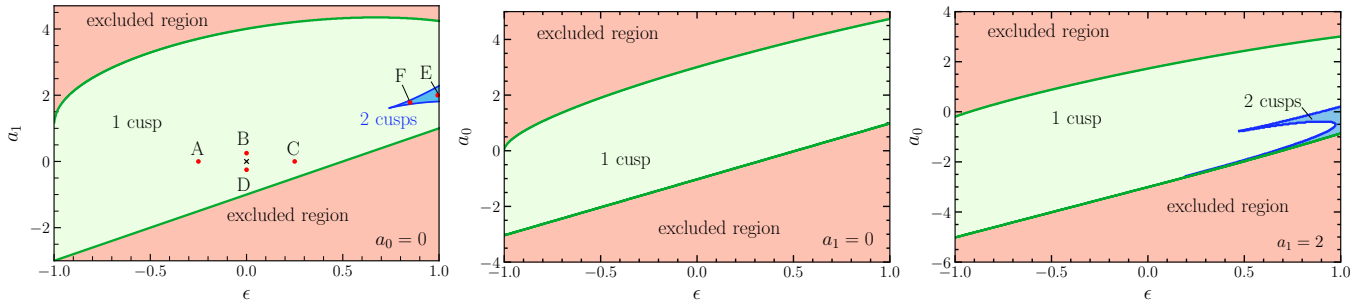


**Figure 2.** Multidimensional parameter space for tori solutions for the three RZ parameters considered here:  $\epsilon$ ,  $a_0$  and  $a_1$ . Shown as green-shaded are the regions where tori can be constructed and these are limited by solid green lines, with the lower one enforcing Eq. (32) and the upper one Eq. (34); no tori solutions can be built in the salmon-shaded regions. From left to right the different panels refer to sections where  $a_0 = 0$ ,  $a_1 = 0$ , and  $a_1 = 2$ , respectively. The blue-shaded areas represent instead the regions where double-tori solutions are possible. Finally, red circles are used to mark the position of the representative models that are discussed in the text, while the black cross marks the position of a Schwarzschild spacetime.

#### 4 SPACE OF SOLUTIONS: SINGLE TORI

Figure 2 shows with different shadings the various regions where solutions as single-torus solutions can be found (green shading) or not (salmon shading). More specifically, the green-shaded area – where solutions are possible – is upper-limited by the condition (20) and lower-limited by the condition (31); in such a region, the specific angular momentum only has a single minimum and the effective potential shows a single cusp. The left panel in Fig. 2 refers to the case when  $a_0 = 0$  and  $a_1 = 2$ , respectively. In what follows (see Sec. 4.1), we will discuss four models in this green region: A, B, C, and D, which are marked by red dots and surround the Schwarzschild solution; the latter obviously corresponds to the case of  $\epsilon = 0$ ,  $a_1 = 0$  and is marked with a black cross. Also shown in Fig. 2 (with a blue-shaded area) is the region in which double-tori solutions are possible. The specific angular momentum here has two minima and one maximum, which allows to distinguish these solutions from the single-torus ones. The effective potential, on the other hand, has two cusps and two maxima, which can be filled with fluid to obtain two tori.

Further below (see Sec. 5), we will also discuss in the double-tori region two models: E, and F. If the fluid in these three models fills up the outermost equipotential surface, then the cusp of the outer torus is connected to the outer edge of the inner torus. Since the models in the middle and right panels of Fig. 2 do not offer specific qualitative differences from those presented in the right panel, they will not be discussed in detail here.

##### 4.1 Single-torus solutions ( $a_0 = 0$ )

As anticipated above, fixing the value of the specific angular momentum allows us to investigate the changes in the potential with the parameters  $\epsilon$  and  $a_1$ . Hence, by suitably choosing the parameters  $\epsilon$ , and  $a_1$ , we are able to construct four representative models,

Model A:	$\epsilon = -0.25$ ,	$a_1 = 0.00$ ,
Model B:	$\epsilon = 0.00$ ,	$a_1 = 0.25$ ,
Model C:	$\epsilon = 0.25$ ,	$a_1 = 0.00$ ,
Model D:	$\epsilon = 0.00$ ,	$a_1 = -0.25$ .

As can be seen from Fig. 3, the shape of the potential changes and, in particular, the left panel contrasts Models A and C (dark and light blue lines) assessing the impact of the parameter  $\epsilon$ , while the right

panel contrasts Models B and D (dark and light red lines) highlighting the impact of the parameter  $a_1$ . In all cases, the Schwarzschild solution is shown as a reference by a black solid line.

From the study of Models A and C it is possible to deduce that for  $\epsilon < 0$  the value of the potential at the cusp and at the maximum of the torus is smaller than the corresponding value in the Schwarzschild spacetime (see, respectively, filled and empty diamonds in the left panel of Fig. 3), since a larger value of the specific angular momentum of  $\ell = 4.35$  for Model A is needed to lift the value of the potential to the one of the Schwarzschild spacetime, which is shown for  $\ell = 3.9$ . At the same time for  $\epsilon > 0$  the opposite is true and the value of the potential is larger than in the Schwarzschild spacetime needing a smaller specific angular momentum of  $\ell = 3.82$  for Model C. In both cases, the position of the cusp,  $r_{\text{cusp}}$ , moves to larger radii when considering the same value of angular momentum.

This can be readily appreciated by inspecting the left and right panels of Fig. 4, which are similar to Fig. 1, and report via a colour-code the effective potential as a function of the radial coordinate  $x$  and of the parameter  $\epsilon$  at a fixed specific angular momentum  $\ell = 4.35$  (left) and  $\ell = 3.82$  (right), and RZ-parameters  $a_0 = 0 = a_1$ . Clearly, the cusp is closest to the horizon for  $\epsilon = 0$ , which corresponds to the Schwarzschild spacetime, and then moves further away (i.e., to larger values of  $x$ ) for increasing  $|\epsilon|$  (orange line). The left and right panels of Fig. 4 also show the position of the maximum-pressure of the torus  $r_{\text{max}}$  and highlight that it shifts to smaller radii for negative  $\epsilon$  and to larger radii for positive  $\epsilon$  as compared to the Schwarzschild solution (purple line). In essence, therefore, for increasing  $\epsilon$ , and independently of its sign, the position  $r_{\text{max}}$  moves to ever larger values of  $x$ . Similarly, the position of the outer radius of the torus  $r_{\text{out}}$  (blue line) increases for increasing values of  $\epsilon$  and in the left panel it reaches spatial infinity at  $\epsilon = -0.21$ , for which the value of the potential at the cusp becomes zero. For larger values  $\epsilon$  the tori would be overfilling their Roche limit and hence no tori in stable equilibrium can be built (see by the bright shaded region with no stable-tori solutions).

Rather similar considerations can be made for Models B and D (see Fig. 5), for which we find that for  $a_1 < 0$  the value of the potential at the cusp is smaller than the value of the potential in the Schwarzschild spacetime and larger for  $a_1 > 0$ . At the same time, the cusp shifts closer to the horizon with increasing  $a_1$  (orange line), while the position and value of the potential at the maximum of the torus changes only slightly with  $a_1$ , increasing with increasing  $a_1$  (purple line). Analogous the position of  $r_{\text{out}}$  moves closer to spatial infinity for increasing  $a_1$ .

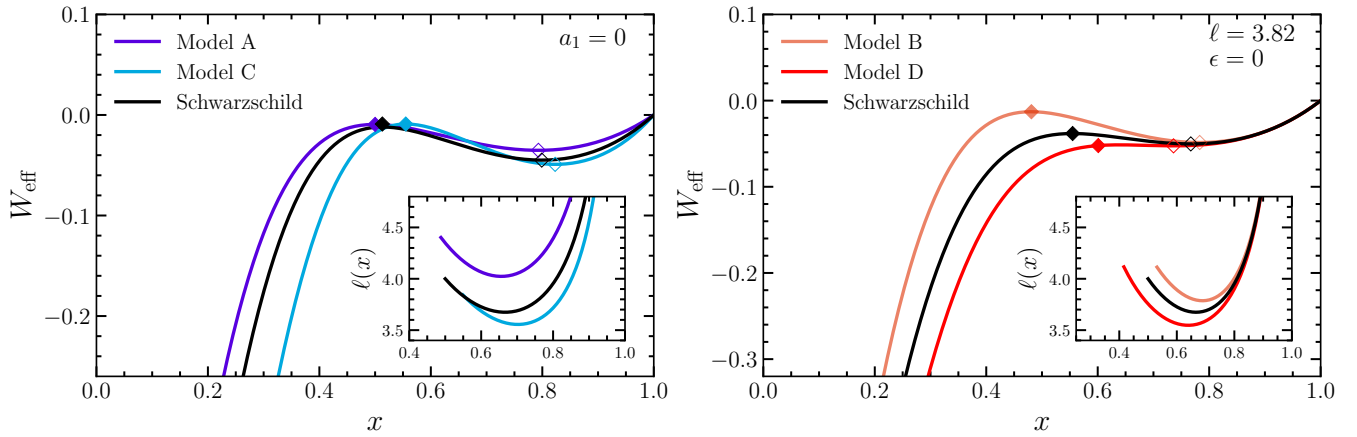


**Figure 3.** *Left panel:* the effective potential at a fixed constant specific angular momentum in units of the ADM-mass  $M$  for Model A at  $\ell = 4.35$  (dark-blue solid line), Model case C (light-blue solid line) at  $\ell = 3.82$ ; also reported is  $W_{\text{eff}}$  in the case of a Schwarzschild spacetime with  $\ell = 3.9$  (black solid line). *Right panel:* the same as in the left but for Model cases B (light-red solid line) and D (dark-red solid line) and the Schwarzschild solution at  $\ell = 3.82$  (black solid line). In both cases we mark with filled (unfilled) diamonds the position of the maximum (minimum) of the effective potential. Finally, shown with insets in both cases is the spatial dependence of the specific angular momentum, which is terminated at the marginally bound orbit.

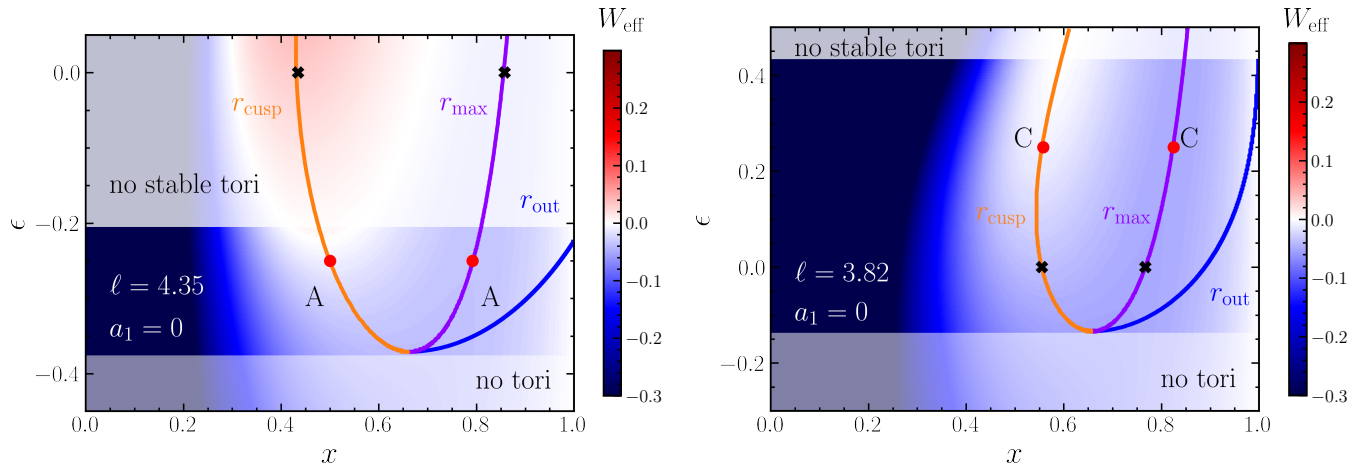


**Figure 4.** *Left panel:* the same as in Fig. 1 but for Model A in a RZ spacetime with parameters  $a_0 = 0 = a_1$ ; in this case the coefficient  $\epsilon$  is varied and the specific angular momentum is kept fixed at the representative value  $\ell = 4.35$ . *Right panel:* the same as in the left panel but Model C and  $\ell = 3.82$ .

Figures 4 and 5 also help to appreciate via the colourcoding that the potential increases for increasing values of the RZ parameters  $\epsilon$  and  $a_1$  and that a single cusp is present for all values of  $a_1$ , but also disappears for sufficiently small and negative values of  $\epsilon$ , i.e., for  $\epsilon \leq -0.302$  for a specific angular momentum of  $\ell = 4.35$  and  $\epsilon \leq -0.135$  for a specific angular momentum of  $\ell = 3.82$  (where the orange and the purple lines meet). Below these values the effective potential shows no cusp and therefore no tori solutions are possible, which is shown by the brighter shaded region. While this behaviour is generic, the value of  $\epsilon$  at which this happens depends on the constant specific angular momentum considered. Finally, marked with red circles in Figs. 4, 5 are the four representative Models A–D and by simply considering the distance in the conformal coordinate  $x$  between the these points it is simple to appreciate that the torus shape can vary considerably when changing the RZ parameters  $\epsilon$  and  $a_1$  and that, as  $a_1$  is increased, the torus cusp and center systematically move-in and out, respectively.

The very different aspects of the tori in the various cases can also be seen from Fig. 6 where we present the equipotential surfaces and

the von Zeipel cylinders for the case of the Schwarzschild spacetime (left panel) and Models C (middle panel) and D (right panel). The equipotential surfaces are constructed for the same value of the specific angular momentum of  $\ell = 3.82$  and are displayed in terms of the Cartesian coordinate  $\bar{x}$  (not to be confused with the conformal coordinate  $x$ ) and  $\bar{z}$ . Compared to the Schwarzschild case we clearly observe that we obtain a much larger torus for Model C and a much smaller torus for Model D. This figure underlines the statement that the size of the torus increases with increasing parameters  $\epsilon$  and  $a_1$ . Model C has the RZ-parameter  $\epsilon = 0.25$  and the torus size increases (especially in the  $\bar{z}$ -direction) when compared to the  $\epsilon = 0$  Schwarzschild case. In contrast, Model D, has a negative  $a_1$  RZ-parameter, the torus is smaller and also less extended vertically. Note that the von Zeipel cylinders have a cusp at different von Zeipel radius  $\mathcal{R}_{\text{vZ}}$ . In the Schwarzschild case, in fact,  $\mathcal{R}_{\text{vZ}}^2 = 5.1975$ , while it is  $\mathcal{R}_{\text{vZ}}^2 = 4.8351$  for Model C and  $\mathcal{R}_{\text{vZ}}^2 = 5.3879$  for Model D.

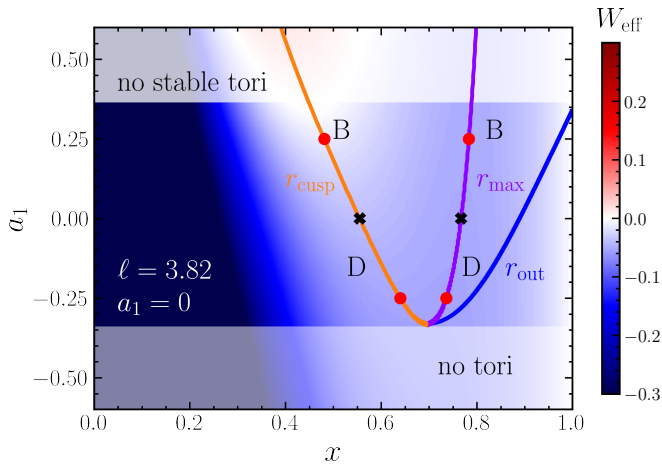


**Figure 5.** The same as in Fig. 4 but for Models B and D in a RZ spacetime with parameters  $\epsilon = 0 = a_0$ ; in this case the coefficient  $a_1$  is varied and the specific angular momentum is kept fixed at the representative value  $\ell = 3.82$ .

## 5 SPACE OF SOLUTIONS: DOUBLE TORI

We next discuss the region of the RZ space of parameters where the specific angular momentum has two minima and the effective potential therefore shows two cusps and two maxima for the *same* constant value of the specific angular momentum. These properties of the effective potential, which *are not* encountered in a Schwarzschild spacetime, lead to what we refer to as “double-tori” solutions.

Within this region, which is shown as blue-shaded in Fig. 2, we consider again two representative model cases obtained after setting  $a_0 = 0$  and suitably selecting the parameters  $\epsilon$  and  $a_1$ , i.e.,

$$\begin{aligned} \text{Model E: } & \epsilon = 1.00, & a_1 = 2.00, \\ \text{Model F: } & \epsilon = 0.85, & a_1 = 1.78. \end{aligned} \quad (38)$$

We should remark that it is in principle possible to build double-tori solutions in a Schwarzschild spacetime and indeed, interesting works exist where these configurations are considered in great detail and where families of nested tori configurations are considered (see, e.g., Pugliese & Stuchlík 2017; Pugliese & Stuchlík 2020). However, in these cases one needs to suitably choose and fine-tune the specific angular momenta – which are *different* for each torus – such that the configuration can actually be built. At the same time, double-tori solutions with the same constant specific angular momentum have been found also in another spherically symmetric black-hole spacetime that is different from the Schwarzschild spacetime, i.e., the  $q$ -metric (Memmen & Perlick 2021).

### 5.1 Double-tori solutions ( $a_0 = 0$ )

When considering Model E, we note that with  $\epsilon = 2.00$  the RZ parameter  $a_1$  needs to be in the range  $1.812 \leq a_1 \leq 2.28$  so that two well-defined cusps can appear in the effective potential, hence our choice of  $a_1 = 2$ . The bottom-left part of Fig. 7 shows the spatial dependence of the specific angular momentum, which clearly exhibits two minima, while the top-left of the same figure shows the effective potential at a fixed angular momentum; the latter,  $\ell = 3.3779$ , has been chosen such that the value of the effective potential at the two cusps is the same. With increasing values of the specific angular momentum, the potential of the inner cusp increases and the potential of the outer cusp decreases; the opposite happens if the specific

angular momentum is decreased. Similarly, when considering Model F, we note that for  $\epsilon = 0.85$  the allowed range for the RZ parameter is  $1.74 \leq a_1 \leq 1.85$  so that two well-defined cusps appear in the effective potential, hence our choice of a representative case with  $a_1 = 1.78$ . Also in this case we display, respectively, in the bottom-right and top-right part of Fig. 7 the spatial dependence of the specific angular momentum and of the effective potential for a fixed value  $\ell = 3.2259$ . Also in this case, and as we will discuss below more in detail, different choices of the constant angular momentum can lead to considerable changes of the effective potential and hence to the appearance (or disappearance) of the outermost cusp.

Figs. 4 and 5 have already illustrated how the changes in the constant specific angular momentum impact on the shape of the effective potential and, in turn, on the properties of the tori. This behaviour becomes made more complex when double-tori solutions are possible and this is demonstrated in Fig. 8, where we concentrate on the representative Model F and again show (with a colourcode) the effective potential for fixed values of  $\ell$  and  $\epsilon$  but varying values of  $a_1$ , while the right panel shows the effective potential for fixed values of  $\ell$  and  $a_1$  but varying values of  $\epsilon$ .

In analogy to Figs. 4 and 5, marked with a transparent map in the left panel of Fig. 8, are those regions where tori solutions are not possible. More specifically, the transparent region at low values of  $a_1$  denotes the range where the specific angular momentum is too small for the effective potential to show a cusp and hence no tori can be constructed there. On the other hand, in the transparent region at high  $a_1$  the tori are unstable because the chosen specific angular momentum is larger than the value at the marginally bound orbit  $\ell > \ell_{\text{mb}}$ . Note that the effective potential has only one cusp for  $1.734 < a_1 < 1.773$ , such that only single-torus solutions are possible in this range of  $a_1$ ; we refer to this region as to the “1-cusp region”, where the positions of the cusps, maxima of the tori and outer radii are presented by solid lines (orange, purple, and blue, respectively) in the 1 cusp region. In the range  $1.773 < a_1 < a_{1,F}$ , where  $a_{1,F} := 1.78$  is the value of  $a_1$  for Model F, a second inner cusp and a second maximum appear in the effective potential at smaller values of  $x$ . In this region, which we refer to as the “2-cusps” region, we mark with solid lines the relevant positions of the innermost (first) torus and with dotted lines of the corresponding colour the various positions of the outermost (second) torus.

In this region, both tori fill their cusps but as the value of  $a_1$  is increased to reach the value of Model F (red dots) the cusps are at the same value of potential for the selected value of  $\ell$ . As a result, for  $a_1 > a_{1,F}$  the potential of the inner cusp increases while the one of the outer cusp decreases. This results in the inner cusp having a value of the effective potential that is larger than the outer cusp and we can no longer obtain two tori filling their cusps. Hence, in the region  $a_{1,F} < a_1 < 1.794$  there are two possibilities to construct tori. The first one is to fill the effective potential up to the inner cusp (solid orange, purple and blue lines), which yields a position of the outer radius larger than the position of the second (outer) cusp and a single extended torus. The second possibility is to fill the effective potential only up to the second (outer) cusp, where the small outer torus (transparent dotted lines) would fill its Roche lobe, but the inner one would not and therefore is not shown. On the other hand, for  $a_1 > 1.794$ , the outer cusp disappears, while the inner (and now only) cusp continues to move to smaller radii, leading to single-torus solutions, which are very extended and again represented by solid lines. Finally, and as mentioned already, the specific angular momentum for parameters  $a_1 > 1.844$  (transparent region) is larger than the marginally bound orbit and the single tori in this region are not in a stable equilibrium and will be subject to accretion.

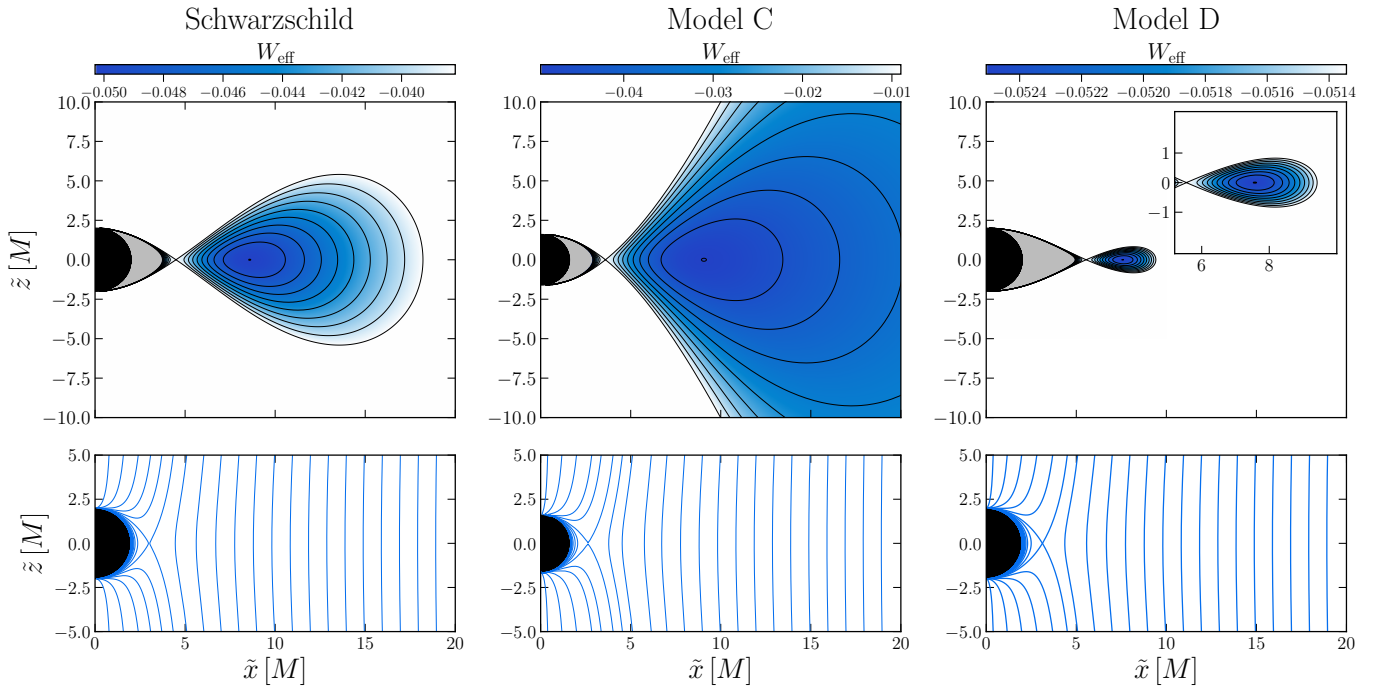


**Figure 6.** Equipotential surfaces of the effective potential (top row) and the von Zeipel cylinders (bottom row) shown in Cartesian coordinates  $\tilde{x}$  and  $\tilde{z}$  and in units of the black-hole mass  $M$ . From left to right the three columns refer to a Schwarzschild spacetime (left), Model C (middle), and Model D (right). Note that the torus in Model C has an outer radius  $r_{\text{out}} = \tilde{x} = 100 M$  and hence cannot be shown in the figure; furthermore, illustrated in an inset in the top-right panel is a magnification of the torus of Model D.

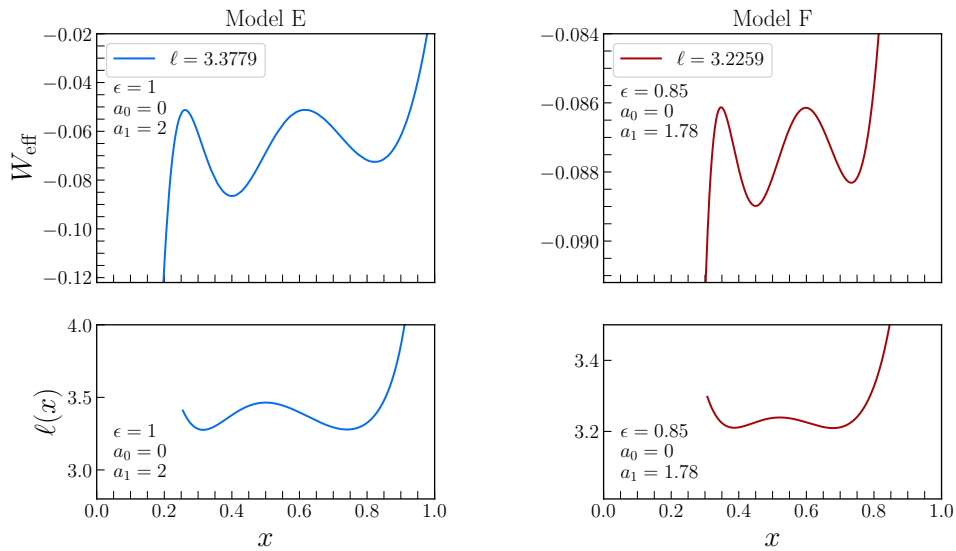


**Figure 7.** Effective potentials at a fixed specific angular momentum (top row) and spatial dependence of the specific angular momenta (bottom row) for Models E (left) and F (right). The effective potentials refer to  $\ell = 3.3779$  for Model E and to  $\ell = 3.2259$  for Model F; these values are chosen so that the two cusps have the same value of  $W_{\text{eff}}$ .

The right panel of Fig. 8, which displays the effective potential at a fixed value of  $a_1 = 1.78$ , but with varying  $\epsilon$  is very similar to the left panel and, indeed, the same considerations apply when going from high to low values of  $\epsilon$ . More specifically, no cusp exists for  $\epsilon > 0.865$  (transparent top region), while a single cusp and maximum (orange and purple solid lines) appear in the region  $0.855 < a_1 < 0.865$  giving rise to single tori.

Two tori filling their cusp are obtained for parameters  $0.85 <$

$\epsilon < 0.855$  with the inner torus represented by solid lines and the outer torus by dotted lines. Model F (marked by red circles) shows two cusps at the same value of the effective potential, while for  $0.845 < \epsilon < \epsilon_F$  the effective potential of the inner cusp rises above the outer one and it is possible to either fill the inner cusp to obtain one large torus (solid lines) or the outer one giving a small outer torus (transparent dotted lines) and an inner one not filling its cusp (not shown). With decreasing value of  $\epsilon$  the outer cusp disappears at

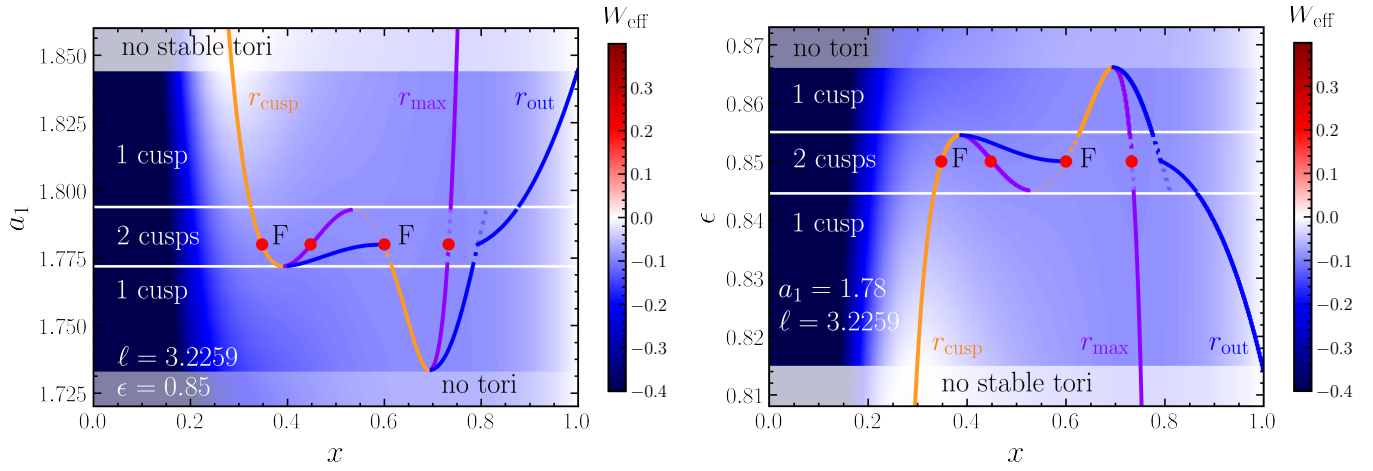


**Figure 8.** *Left panel:* the same as in Fig. 4 but for Model F in a RZ spacetime with parameters  $\epsilon = 0.85$ ,  $a_0 = 0$ ,  $a_1 = 1.78$ ; in this case the coefficient  $a_1$  is varied and the specific angular momentum is kept fixed at the representative value  $\ell = 3.2259$ . The convention for the various lines is the same as in the previous similar representations of the effective potential with the addition that we show by dotted transparent lines the situations in which one or two tori can exist depending on how the equipotential surfaces are filled. Note that in this case double-tori solutions are possible. *Right panel:* the same as in the left panel but where the RZ-parameter  $\epsilon$  is allowed to vary at fixed  $a_1 = 1.78$ .

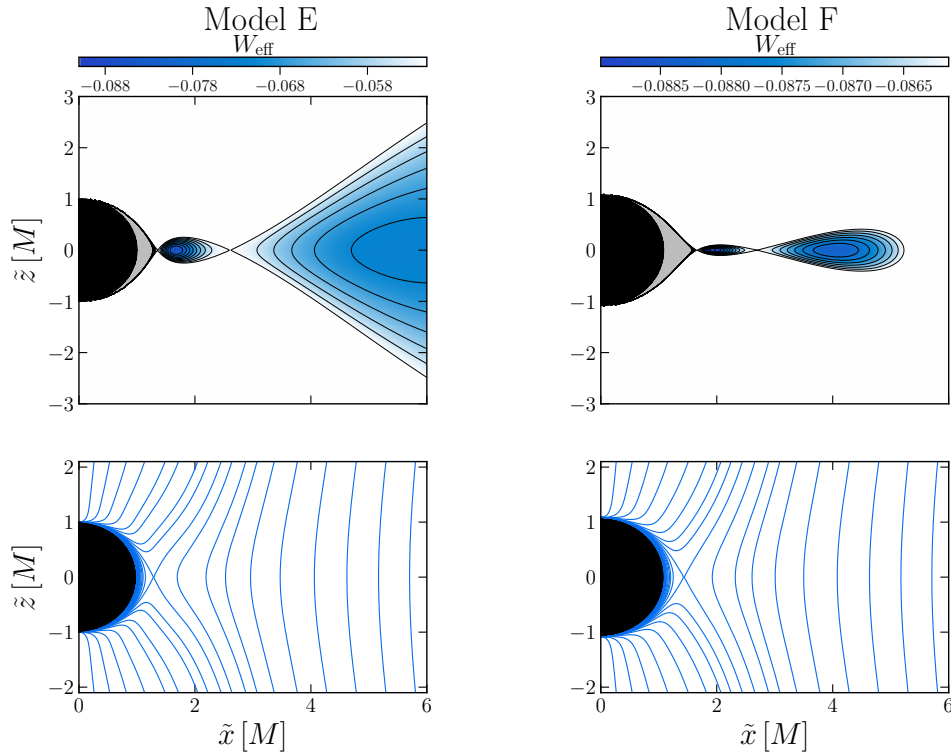


**Figure 9.** The same as in Fig. 6 but for Model E (left) and Model F (right). Note that in both cases two tori are possible and that in the case of Model E the outer torus is much larger than the inner one (the outer radius at  $r_{\text{out}} = \tilde{x} = 13.793 M$ ) and hence is shown only close to the second cusp.

the white solid line and we are left with a single large torus (solid orange, purple and blue lines) in the region  $0.8147 < \epsilon < 0.845$ . Finally, for even smaller values  $\epsilon < 0.8147$  (transparent shading) no tori in stable equilibrium can be obtained since the specific angular momentum is above that of the marginally bound orbit.

Fig. 9 provides a more direct representation of the properties of the tori in Models E (left column) and F (right column) by showing, in analogy to Fig. 6, the equipotential surfaces (top row) and the

von Zeipel cylinders (bottom row). Since Models E (left column) and F (right column) differ essentially in the values of the parameter  $\epsilon$ , Fig. 9 shows that for an increasing value of  $\epsilon$  also the size of the tori increases. Note also the outer torus is systematically larger than the inner one and grows (shrinks) faster with increasing (decreasing)  $\epsilon$ . Overall, the examples discussed in this section highlight that double-tori solutions can be easily obtained in RZ spacetime with  $a_0 = 0$  and in a suitably chosen range of values for  $\epsilon$  and  $a_1$ , which

determine their properties in terms of vertical thickness and size. More importantly, these tori can be filled with fluids having the same constant specific angular momentum and hence are potentially easier to produce in nature as one expects that the matter sourcing these tori near supermassive black holes has the same astrophysical origin and hence the same specific angular momentum. Double-tori solutions are also possible to be constructed in general relativity but, in contrast, require *different* and suitably tuned values of the specific angular momentum for each torus (Pugliese & Stuchlík 2017).

As a final remark we note that while the effective potential in the case of double-tori solutions has two distinct cusps, the von Zeipel radius can only have one cusp and this has to necessarily appear close to the black hole and not at large distances (see Fig. 9). This is because  $W_{\text{eff}}$  depends on both the  $g_{tt}$  metric function and on the specific angular momentum [see Eq. (23)]; while the former does not have extrema at large distances from the black hole, the latter does, as shown for instance in Fig. 7. By contrast, the von Zeipel radius depends only on the  $g_{tt}$  metric function and thus has a only one local minimum at the photon ring, while approaching asymptotic flatness at large distances [see Eq. (22)].

## 6 CONCLUSIONS

The study of non-selfgravitating equilibrium tori orbiting around black holes has a long history and these models have found a number of applications in the simulation of accretion flows onto black holes and other compact objects. We have revisited the problem of constructing such equilibria starting from the simplest black-hole spacetimes, i.e., spherically symmetric, but expressed in terms of a fully generic and rapidly converging parameterisation: the RZ metric.

Already in general relativity, the construction of such equilibria does not depend on the  $g_{rr}$  metric function and thus our analysis has been restricted to the first three parameters of the  $g_{tt}$  metric function within the RZ metric, i.e.,  $\epsilon$ ,  $a_0$  and  $a_1$ . Within this framework we have extended the definitions of all of the quantities characterising these equilibria, starting from the concept of the von Zeipel cylinders and up to the possible ranges of the specific angular momenta that are employed to construct families of tori.

In this way, we were able to set precise constraints on the ranges of the RZ coefficients and thus define the space of parameters in which tori solutions are possible and those where no such solutions can be constructed. To make our analysis more tractable, we have further assumed that  $a_0 = 0$  (as in general relativity) since this is the coefficient that is best constrained by parameterised post-Newtonian measurements to be  $a_0 \lesssim 10^{-4}$ . Within the allowed space of parameters we have then encountered both standard “single-torus” solutions, but also non-standard “double-tori” solutions. While the properties of the first ones in terms of the presence of a single cusp, of a local pressure maximum and of a varying outer radius, are very similar to those encountered in general relativity, the properties of double-tori solutions are far richer. In particular, depending on the specific region of the space of parameters, it is possible to construct tori that have two cusps and fill the corresponding equipotential surfaces either up to the value of the effective potential at the first cusp or at that of the second cusp. In this way, transitions from single-torus to double-tori solutions (and vice-versa) are possible and the RZ parameterisation opens therefore the way to the exploration of a much richer class of equilibria than in general relativity. More importantly, these tori can be filled with fluids having the *same* constant specific angular momentum and hence are potentially easier to produce in nature as one expects that the matter sourcing these tori close to supermassive

black holes has the same astrophysical origin and hence the same specific angular momentum.

A concluding remark should be dedicated to the plausibility of these solutions. Of course, all present observations of black holes, either via gravitational waves (The LIGO Scientific Collaboration & the Virgo Collaboration 2016) or via imaging (Event Horizon Telescope Collaboration et al. 2019, 2022a) portray a picture that is perfectly compatible with general relativity, which still represents the best theory of gravity presently available. At the same time, observations are sufficiently uncertain to leave room for alternative theories and for deviations from general relativity. If cast in this context, and when supported by precise astronomical observations, the existence of these equilibrium tori would provide very valuable information on the properties of the spacetime and on its deviation from general relativity.

## ACKNOWLEDGMENTS

It is a pleasure to thank A. Cruz-Osorio, C. Ecker, and P. Kocherlakota for useful discussions and comments. Support in funding comes from the State of Hesse within the Research Cluster ELEMENTS (Project ID 500/10.006), from the ERC Advanced Grant “JETSET: Launching, propagation and emission of relativistic jets from binary mergers and across mass scales” (Grant No. 884631).

## DATA AVAILABILITY

Data available on request. The data underlying this article will be shared on reasonable request to the corresponding author.

## REFERENCES

- Abdikamalov A. B., Ayzenberg D., Bambi C., Nampalliwar S., Tripathi A., 2021, *Phys. Rev. D*, 104, 024058
- Abramowicz M. A., 1971, *Acta Astronomica*, 21, 81
- Abramowicz M. A., Fragile P. C., 2013, *Living Rev. Relativity*, 16
- Abramowicz M., Jaroszynski M., Sikora M., 1978, *Astron. Astrophys.*, 63, 221
- Bauer A., Cárdenas-Avendaño A., Gammie C. F., Yunes N., 2021, arXiv e-prints, p. arXiv:2111.02178
- Blandford R. D., Znajek R. L., 1977, *Mon. Not. R. Astron. Soc.*, 179, 433
- Bronnikov K. A., Konoplya R. A., Pappas T. D., 2021, *Phys. Rev. D*, 103, 124062
- Cardoso V., Pani P., Rico J., 2014, *Phys. Rev. D*, 89, 064007
- Cruz-Osorio A., Gimeno-Soler S., Font J. A., De Laurentis M., Mendoza S., 2021, *Phys. Rev. D*, 103, 124009
- Event Horizon Telescope Collaboration et al., 2019, *Astrophys. J. Lett.*, 875, L1
- Event Horizon Telescope Collaboration et al., 2022a, *Astrophys. J. Lett.*, 930, L12
- Event Horizon Telescope Collaboration et al., 2022b, *Astrophys. J. Lett.*, 930, L17
- Faraji S., Trova A., 2021, *Astron. Astrophys.*, 654, A100
- Fishbone L. G., Moncrief V., 1976, *Astrophys. J.*, 207, 962
- Font J. A., Daigne F., 2002, *Mon. Not. R. Astron. Soc.*, 334, 383
- Gimeno-Soler S., Font J. A., Herdeiro C., Radu E., 2019, *Phys. Rev. D*, 99, 043002
- Gimeno-Soler S., Font J. A., Herdeiro C., Radu E., 2021, *Phys. Rev. D*, 104, 103008
- Jeřemov P., Perlick V., 2016, *Class. Quant. Grav.*, 33, 245014
- Kocherlakota P., Rezzolla L., 2020, *Phys. Rev. D*, 102, 064058
- Kocherlakota P., Rezzolla L., 2022a, arXiv e-prints, p. arXiv:2206.03146

- Kocherlakota P., Rezzolla L., 2022b, *Mon. Not. R. Astron. Soc.*, 513, 1229
- Kocherlakota P., et al., 2021, *Phys. Rev. D*, 103, 104047
- Kokkotas K. D., Konoplya R. A., Zhidenko A., 2017, *Phys. Rev. D*, 96, 064007
- Konoplya R. A., Zhidenko A., 2020a, *Phys. Rev. D*, 101, 124004
- Konoplya R. A., Zhidenko A., 2020b, *Phys. Rev. D*, 101, 124004
- Konoplya R. A., Zhidenko A., 2022, *Phys. Rev. D*, 105, 104032
- Konoplya R., Rezzolla L., Zhidenko A., 2016, *Phys. Rev. D*, 93, 064015
- Konoplya R. A., Pappas T. D., Stuchlík Z., 2020, *Phys. Rev. D*, 102, 084043
- Konoplya R. A., Kunz J., Zhidenko A., 2021, *JCAP*, 12, 002
- Kovar J., Slany P., Stuchlík Z., Karas V., Cremaschini C., Miller J. C., 2011, *Phys. Rev. D*, 84, 084002
- Kozłowski M., Jaroszynski M., Abramowicz M. A., 1978, *Astron. and Astrophys.*, 63, 209
- Kučáková H., Slany P., Stuchlík Z., 2011, *Journal of Cosmology and Astroparticle Physics*, 2011
- Meliani Z., Vincent F. H., Grandclément P., Gourgoulhon E., Monceau-Baroux R., Straub O., 2015, *Class. Quant. Grav.*, 32, 235022
- Memmen J.-M., Perlick V., 2021, *Class. Quant. Grav.*, 38, 135002
- Nampalliwar S., et al., 2020, *Phys. Rev. D*, 102, 124071
- Ni Y., Jiang J., Bambi C., 2016, *Journal of Cosmology and Astroparticle Physics*, 1609, 014
- Olivares H., et al., 2020, *MNRAS*, 497, 521
- Porth O., et al., 2019, *Astrophys. J. Suppl.*, 243, 26
- Pugliese D., Stuchlík Z., 2017, *Astrophys. J. Suppl.*, 229, 40
- Pugliese D., Stuchlík Z., 2020, *Class. Quant. Grav.*, 37, 195025
- Rezzolla L., Zanotti O., 2013, *Relativistic Hydrodynamics*. Oxford University Press, Oxford, UK, doi:10.1093/acprof:oso/9780198528906.001.0001
- Rezzolla L., Zhidenko A., 2014, *Phys. Rev. D*, 90, 084009
- Rezzolla L., Yoshida S., Maccarone T. J., Zanotti O., 2003a, *Mon. Not. R. Astron. Soc.*, 344, L37
- Rezzolla L., Zanotti O., Font J. A., 2003b, *Astron. Astrophys.*, 412, 603
- Shashank S., Bambi C., 2022, *Phys. Rev. D*, 105, 104004
- Siqueira P. H. C., Richartz M., 2022, *Phys. Rev. D*, 106, 024046
- Stuchlík Z., Slany P., Kovar J., 2009, *Class. Quant. Grav.*, 26, 215013
- Stuchlík Z., Pugliese D., Schee J., Kučáková H., 2015, *Eur. Phys. J. C*, 75, 451
- Suvorov A. G., Völkel S. H., 2021a, *Phys. Rev. D*, 103, 044027
- Suvorov A. G., Völkel S. H., 2021b, *Phys. Rev. D*, 103, 044027
- Tassoul J.-L., 2007, *Stellar Rotation*
- Teodoro M. C., Collodel L. G., Kunz J., 2021a, *JCAP*, 03, 063
- Teodoro M. C., Collodel L. G., Doneva D., Kunz J., Nedkova P., Yazadjiev S., 2021b, *Phys. Rev. D*, 104, 124047
- The LIGO Scientific Collaboration the Virgo Collaboration 2016, *Phys. Rev. Lett.*, 116, 221101
- Völkel S. H., Kokkotas K. D., 2019, *Phys. Rev. D*, 100, 044026
- Völkel S. H., Barausse E., Franchini N., Broderick A. E., 2020, arXiv e-prints, Will C. M., 2006, *Living Rev. Relativity*, 9, 3
- Witzany V., Jefremov P., 2018, *Astron. Astrophys.*, 614, A75
- Younsi Z., Zhidenko A., Rezzolla L., Konoplya R., Mizuno Y., 2016, *Phys. Rev. D*, 94, 084025
- Yu Z., Jiang Q., Abdikamalov A. B., Ayzenberg D., Bambi C., Liu H., Nampalliwar S., Tripathi A., 2021, *Phys. Rev. D*, 104, 084035
- Çikintoğlu S., Ekşi K. Y., Rezzolla L., 2022, *MNRAS*, 517, 3212
- von Zeipel H., 1924, *Mon. Not. Roy. Soc.*, 84, 665

This paper has been typeset from a  $\text{\TeX}/\text{\LaTeX}$  file prepared by the author.